



Retinal blood vessel segmentation using pixel-based feature vector



Buket Toptaş^{a,*}, Davut Hanbay^b

^a Computer Eng. Dept., Engineering and Natural Science Faculty, Bandırma Onyedi Eylül University, Balıkesir, Turkey

^b Computer Eng. Dept., Engineering Faculty, Inonu University, 44280 Malatya, Turkey

ARTICLE INFO

Keywords:

Biomedical imaging
Retinal blood vessel segmentation
Image segmentation
Feature extraction

ABSTRACT

A lot of important disease information can be accessed by performing retinal blood vessel analysis on fundus images. Diabetic retinopathy is one of the diseases understood by retinal blood vessel analysis. If this disease is detected at an early stage, vision loss can be prevented. In this paper, a method that performs retinal blood vessel analysis with classical methods is proposed. In this proposed system, pixel-based feature extraction is performed. Five different feature groups are used for feature extraction. These feature groups are edge detection, morphological, statistical, gradient, and Hessian matrix. An 18-D feature vector is created for each pixel. This feature vector is given to the artificial neural network for training. Using test images, the system is tested on two publicly available datasets. Sensitivity, Specificity, and Accuracy performance measures were used as success measures. The similarity index between the segmented image and the ground truth is measured using Dice and Jaccard. The accuracy of the system was measured as 96.18% for DRIVE and 94.56% for STARE, respectively. Experimental results show that the proposed algorithm achieves satisfactory results. This method can be used as an automated retinal blood vessel segmenting system.

1. Introduction

Computer-aided systems (CAD) are widely used in the medical field. CADs are preferred because they give robust, accurate, and fast results. Also, CADs alone do the work of many experts. Thus, it minimizes errors caused by human negligence. One of the CADs is fundus image analysis. Using fundus images can be detected fields such as optic disc [1–4], optic cup [5–8], fovea [9–12], macula [13,14], exudate [3,4,15–17] and blood vessels [18–22].

Automated segmentation of retinal blood vessels is an important step for computer-aided fundus image analysis. Many diseases such as age-related macular degeneration [23,24], glaucoma [25,26], diabetes [27–31] and hypertension [32–34] can be detected using the retinal blood vessel in the fundus image. With the increasing number of these diseases, the variety of retinal vascular segmentation methods has also increased.

In literature are generally presented various computer-aided methods for diseases by using features such as the branching angle, width of the retinal vessel, and the calibrated curvature of the retinal vessel. Beaudelaire et al. [35] proposed a vessels segmentation method based on the classical edge detection filters and artificial neural networks. In their method, they used edge detection filters to extract the

feature vector. The extracted features are given as an introduction to an artificial neural network to understand whether each pixel belongs to blood vessels. Orujov et al. [36] enhanced an image processing algorithm for the detection of blood vessels in retinal fundus images. In this algorithm, Mamdani (Type-2) fuzzy rules are used. Jebaseeli et al. [37] proposed the system for retinal blood vessel segmentation. The proposed system uses Tandem Pulse Coupled Neural Network (TPCNN) model for automatic feature vector creation and then Deep Learning-Based Support Vector Machine (DLBSVM) for classification and extraction. The TPCNN model operates on inter and intra channel linking of the input neurons. Wang et al. [38] proposed a new cascade classification framework for retinal vessel segmentation. Vessel segmentation consists of Mahalanobis distance classifiers to form an extremely nonlinear decision. Mahalanobis distance is computationally efficient. Here, network size is not defined in advance but is determined by the complexity of the training data. Ramos et al. [39] reduce the noise of the green channel of the original image using a Low-Pass Radius Filter. Then, a 30-element Gabor filter and a Gaussian fractional derivative are used to notably enhance the vascular segmentation. Finally, a threshold method and morphological process are applied to isolate the vascular structure. The method proposed by Zhu et al. [40] is based on Extreme Learning Machine (ELM) for segmentation of retinal vessels. In the training step, a

* Corresponding author.

E-mail addresses: btoptas@bandirma.edu.tr (B. Toptaş), davut.hanbay@inonu.edu.tr (D. Hanbay).

Table 1

Feature vector of each pixel.

No.	Feature (dimension)	Feature description
1	Edge Algorithm (1)	Sum (Roberts, Prewitt, Sobel, Canny, Log)
2	Morphological (2)	Bot-hat transformation, Top-hat transformation
3	Statistical Feature (8)	Mean, Minimum, Maximum, Skewness, Kurtosis, Standard deviation, Mean absolute deviation, Root sum of squared level
4	Gradient-Based Features (4)	1st derivative Horizontal Gradient Ix, 1st derivative Vertical Gradient Iy, Gradient Vector Magnitude, Gradient Direction
5	Hessian-Matrix Features (3)	2st derivative Gxx, 2st derivative Gxy, 2st derivative Gyy

feature vector is created for each pixel of the training retinal image. This feature vector consists of morphological progress, Hessian matrix, local intensity, and divergence of vector fields. To obtain a classifier is used the feature vector and manual labels. Rezaee et al. [41] suggested an efficient method based on Fuzzy Entropy. Firstly, the blurring noises are eliminated with a Wiener filter provided. Secondly, the adaptive filter is used and blood vessels are extracted at a basic level. Rodrigues et al. [42] proposed a method using wavelets, Hessian, and morphology. In this method, both optical disc detection and retinal vascular network structure were determined. Researchers worked on the tubular characteristic of the retinal blood vessel to determine veins and arteries. Cuevas et al. [43] implemented a method called Lateral Inhibition (LI) on the retinal images. LI is a technique inspired by nature. The author's goal is to improve the contrast between the retinal vessels and the background of the image. Also, it is decided whether an image pixel belongs to the blood vessel by finding a suitable threshold value. For the threshold value, the Differential Evolution (DE) algorithm based on cross-entropy is used. Khan et al. [44] improved an effective method for automatically extracting blood vessels from color retinal images. This method relies on an edge operator. Edge operator is called the name normalized Gaussian Derivative Kernel in the second order. Principal component analysis-based image preprocessing is applied to the images before this operator is applied to the images. Sigursson et al. [45] presented a method based on feature extraction for the detection of blood vessels in the retinal images. This presented method focused on two vessel features. The first feature is extracted using the local minimum detection method. The second feature is extracted using the edge detection method. Nayebifar et al. [46] proposed a novel method that relies on particle filters. The purpose of the authors is to determine and locally track the vessel paths in the retinal image. The method uses a probability density function (PDF). Firstly, optic disc localization is determined. Then a recursive tracking process begins using an appropriate set of starting points. Chaudhuri et al. [47] presented an MF filter based on optical and spatial properties of vessels to be recognized. MF was built on assumption. In this assumption, the gray-level profile of the cross-section of the vessel is thought to be the shape of Gaussian. The authors created a set of 12 templates that are used to match the vessels along with the different directions. However, MF may vary in many ways rely on the parameters. Al-Rawi et al. [48] optimized the parameters of MF using a genetic algorithm. Cinsdikici et al. [49] optimized the parameters of MF using an ant colony algorithm. Sreejini et al. [50] optimized the parameters of MF using a particle swarm optimization algorithm.

One of the main problems of blood vessel segmentation in retinal fundus images is poor image quality. Thus, in literature generally applied enhancement methods before retinal vessel segmentation were performed. In this paper, the contrast limited adaptive histogram equalization (CLAHE) method is used in the preprocessing stage. The CLAHE method is one of the most popular preprocessing methods used on retinal fundus images [51–55]. A median filter was applied to images after the CLAHE method. The Median filter is used to reduce other noise

on the preprocessed image. After the preprocessing stage, the feature vector generation stage begins. The feature vector is created by subtracting 18-D features from each pixel of the preprocessed image. The data set is trained using these features. Artificial Neural Network (ANN) is used in the training stage. After the training stage, the test process starts. Thus, the pixel-based retinal vessel segmentation process is realized. In the proposed method, an accuracy rate of 0.9618 was obtained for the DRIVE data set, and an accuracy rate of 0.9456 was obtained for the STARE data set.

This paper focuses on using classic features effectively. The critical contributions are as follows:

- Instead of all traditional edge detection methods, this paper presents these methods combined as a single feature.
- The statistical properties are presented in a different technique to increase the robustness of the vessel segmentation.
- The proposed method was built independently from the database.

The organization of the rest of this paper is as follows: Material and details of the method are presented in Section 2. Experimental results and discussion of the proposed method are given in Section 3. Finally, the conclusion is given in Section 4.

2. Materials and methods

The proposed method presents a vessel segmentation method by extracting pixel-based features on retinal images. In the proposed method, there is a preprocessing stage first. A pixel-based feature vector has been extracted on the preprocessed images. The created feature vector has been given as an input to the ANN. Testing is performed after the ANN is trained. The testing process has been carried out on public datasets. The created feature vector for each pixel is given in Table 1. The block diagram of the proposed method is given in Fig. 1.

2.1. Pre-Processing

The preprocessing stage is applied to the entire rectangle image, but operations are made on the Region of Interest (ROI) in this article. Because only ROI pixels are used for vessel detection. The useless pixels associated with the dataset image (i.e dark pixels outside the ROI area) are removed from the image to speed up the further processing steps. To create the retinal ROI, the mask images given inside the dataset of DRIVE (i.e FOV mask images given in the dataset) are used to determine the ROI region in this dataset. STARE dataset does not contain ready-made mask images, unlike the DRIVE dataset. In this article, the mask images of the STARE data set are created manually. The retinal images may suffer from both non-uniform illumination and poor quality, thus before extraction of blood vessels preprocessing is necessary. The preprocessing stage significantly can change the segmentation result. The preprocessing steps used are as follows: mathematical morphological opening operator, contrast limited adaptive histogram equalization, and median filtering.

Central light reflexes can be found in retinal images due to the different light intensity. Normally, a blood vessel has a single centerline and two edges. However, a blood vessel containing a central light reflex behaves as if there were two separate vessels. In order to eliminate this problem, the morphological opening process is applied on the green channel. A disk of radius 2 is used as the structural element. A light reflex image is shown in Fig. 2. Then, contrast limited adaptive histogram equalization (CLAHE) algorithm is applied for enhancing the image. CLAHE benefits in enhancing the contrast between objects and the background of the image. Thus, the contrast between the vessels and the background is increased. After applying CLAHE, a median filter is applied to the images. Median filter softens noises and eliminates salt and pepper noises. A preprocessed dataset image is shown in Fig. 3.

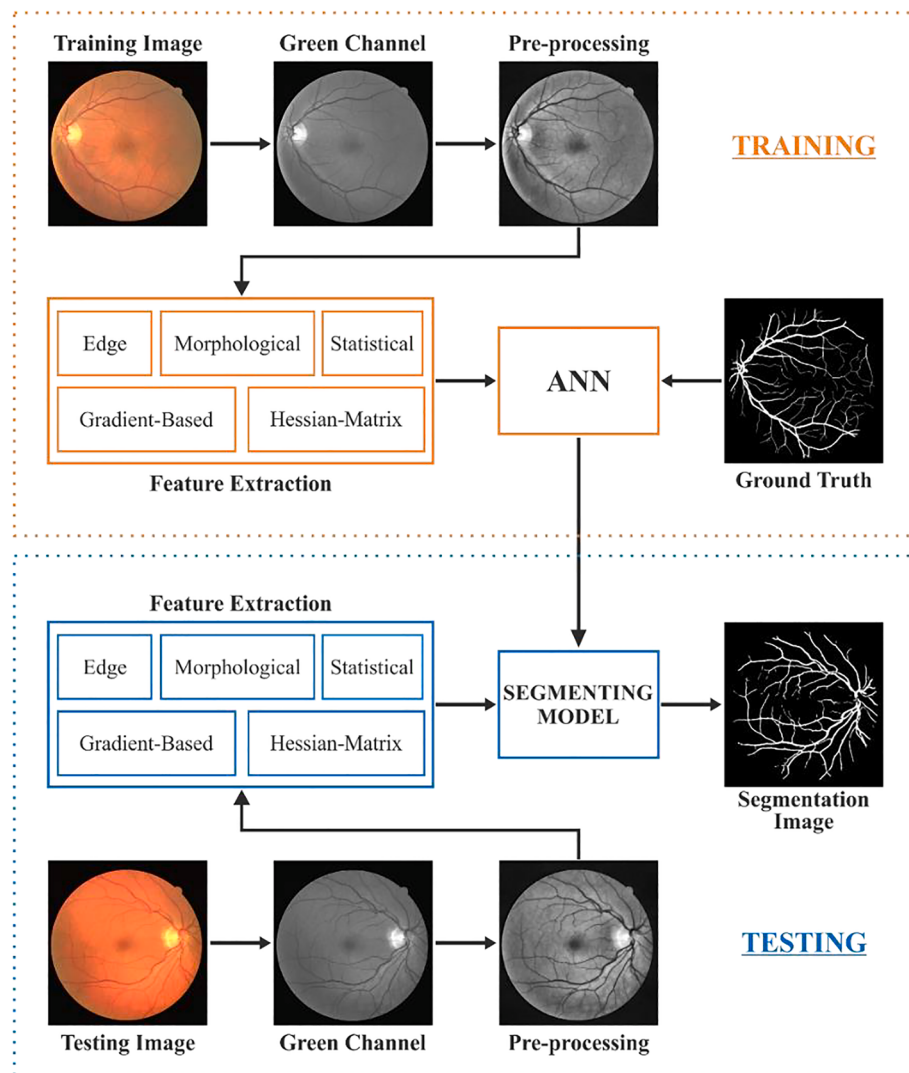


Fig. 1. Block diagram of the proposed method.

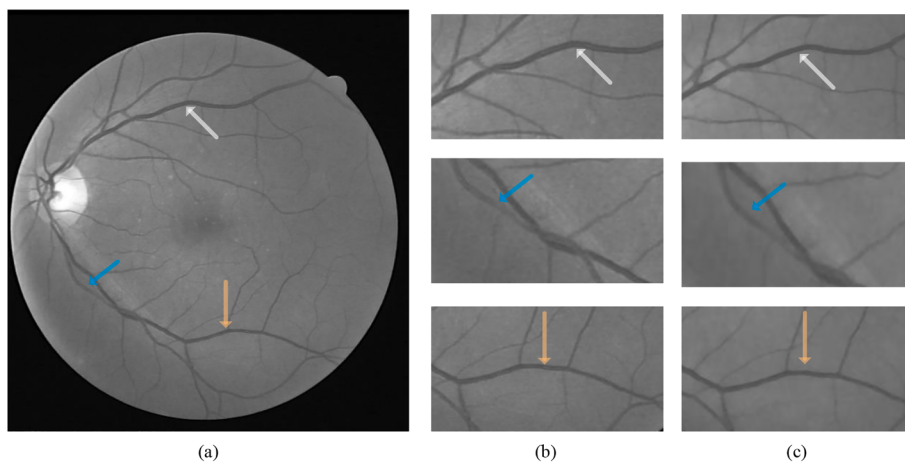


Fig. 2. A light reflex image. (a) Light reflex in the non-preprocessed image, (b) Corrected vessels after an opening process.

2.2. Feature vector

2.2.1. Edge operators (One feature)

Edges are sudden gray-level changes in the image and contain a lot of

important information that belongs to the image. There are a number of methods to perform edge detection. Five different edge detection operators are used in this article. These five different edge detection methods have been applied to fundus images and edges of the vessels in the image

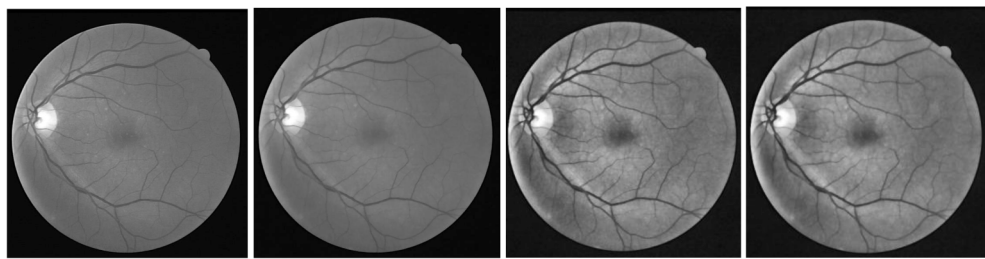


Fig. 3. Pre-processing stages. The first image is the green channel image. The second image is the opening process application result. The third image is the CLAHE result. The result of the preprocessing image.

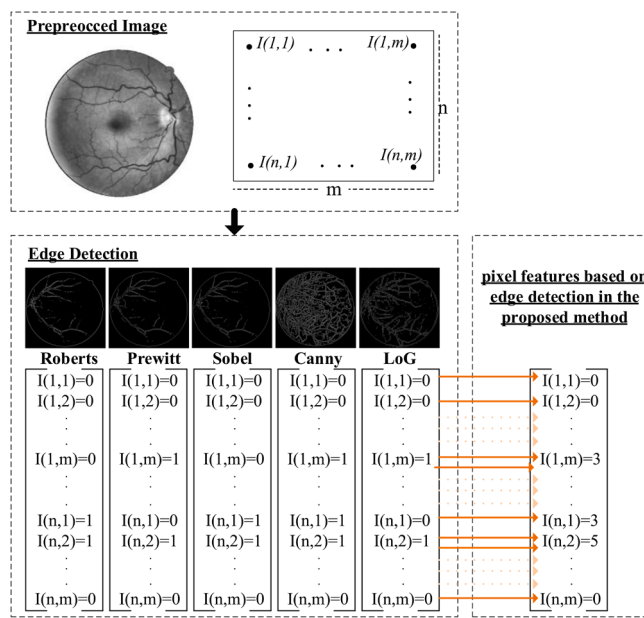


Fig. 4. Feature extraction steps from edge algorithms.

are detected. A single feature vector was obtained by interpreting the pixel-based features obtained by five different edge detection methods. For example, if there is a pixel that is accepted as an edge in all five methods, the feature of that pixel is accepted as 5. So the probability of blood vessel is further emphasized in the final feature vector. Also, classification training is accelerated by using one feature vector representing these features instead of five feature vectors. As a result, 1 (one) feature pixel-based has been extracted from edge detection methods. The results of this process are shown in Fig. 4. The edge operators used are as follows.

Roberts: The Robert filter simply and quickly calculates the gradient value and specifies the high-frequency region expressing edge information. This filter calculates the gradient vector by moving a 2x2 size mask over the image. The gradient vector found is approximated. The gradient is obtained by the convolution of the mask in horizontal and vertical directions on the image. These masks are obtained by the differential equations of the first derivative. The Robert operator is given in Eq. 1 as horizontal (G_x) and vertical (G_y). The G_x filter indicates that the pixels move into the high contrast region. The G_y operator does the same in the 90-degree horizontal direction [56].

$$G_x = \begin{bmatrix} 1 & 0 \\ 0 & -1 \end{bmatrix} \text{ and } G_y = \begin{bmatrix} 0 & 1 \\ -1 & 0 \end{bmatrix} \quad (1)$$

Prewitt: The Prewitt edge detection filter computes the gradient vector at each pixel on the image. The gradient is obtained by convoluting the horizontal and vertical masks on the image. The filter operators are given in Eq. (2). In the G_x operator, the second column is all

zero. Therefore, it detects vertical edges on the image. The second row in the G_y operator is completely zero. Therefore, it detects horizontal edges on the image.

$$G_x = \begin{bmatrix} -1 & 0 & 1 \\ -1 & 0 & 1 \\ -1 & 0 & 1 \end{bmatrix} \text{ and } G_y = \begin{bmatrix} -1 & -1 & -1 \\ 0 & 0 & 0 \\ 1 & 1 & 1 \end{bmatrix} \quad (2)$$

Sobel: The Sobel filter is one of the most popular edge detection filters. It is structurally similar to the Prewitt filter. The only difference is, the filter value in the second row in the horizontal direction and the filter value in the second column in the vertical direction are 2 instead of 1.

The Sobel filter reveals semantic high-frequency regions (i.e., sharp edges) that correspond to the edges of the image. In Eq. (3), a 3x3 filter matrix of the Sobel filter is given.

$$G_x = \begin{bmatrix} -1 & 0 & 1 \\ -2 & 0 & 2 \\ -1 & 0 & 1 \end{bmatrix} \text{ and } G_y = \begin{bmatrix} -1 & -2 & -1 \\ 0 & 0 & 0 \\ 1 & 2 & 1 \end{bmatrix} \quad (3)$$

Canny: The Canny filter targets three main purposes. First, the goal is to detect all edges. It is then that the difference between the possible edge zone and the actual edge zone is kept to a minimum. Finally, it aims to select the correct edge point of one point between the edge points. Basically, the algorithm steps are as follows: Smoothing the image with Gauss, suppressing the non-maximum neighborhood pixel in the filter, threshold.

LoG: The LoG edge detection algorithm uses a Gaussian low pass filter. Thus, it can limit the image in different cut frequencies. In LoG, the image is first convoluted with the Gaussian function and then the laplacian is calculated. Calculation of direct laplacian can result in obtaining many artificial edge points which are undesirable. To prevent this situation, Gaussian was applied to the image first. The 2-D Gauss function used for this purpose is given in Eq. (4).

$$h(x, y) = e^{-\left(\frac{x^2+y^2}{2\sigma^2}\right)} \quad (4)$$

where, x and y operators represent the image coordinates. σ operator represents the Gauss function standard deviation.

2.2.2. Mathematical morphology (Two feature)

Mathematical morphology (MM) operators are one of the most popular methods preferred the preprocess, segmentation, or post-process. The purpose of this method is to protect the basic features of the image and to remove foreign elements from the image. There are basically two morphological operators. These are dilation and erosion operations. The dilation operator connects the discrete regions formed in the images and fills the holes. The erosion operator can diminish objects in the image, separate linked objects, and widen holes. If the dilation operator is used after the erosion operator, the opening operator created. Also, if the erosion operator is used after the dilation operator, the closing operator created. When MM is applied to images it needs a structuring element (SE). The structuring element can be of different

shapes and sizes. These have a central point, and each pixel of the image to be processed is placed on this point. In this article, morphological top-hat transformation and morphological bottom-hat transformation are extracted from the retinal blood vessel image as two different features. Top-hat and bottom-hat transformations are used to provide clarity to blood vessels that have minimal effect on the background intensity level. Top-hat transformation behaves like a high pass filter. For this reason, it extraction the bright areas of the image that are smaller than the mask. The bottom-hat transformation affects the background of the image. In other words, it becomes effective on some dark areas of the image that are smaller than the background mask. Top-hat is given in Eq. (5) and bottom-hat is given in Eq. (6).

$$T_{\text{hat}}(I) = I - (I^{\circ} \text{SE}) \quad (5)$$

$$B_{\text{hat}}(I) = (I \bullet \text{SE}) - I \quad (6)$$

where, I operator represents gray-level fundus image. SE operator represent structural operator. \bullet denote is closing operator. \circ denote is opening operator. The structural element measures 11 pixels long 1 pixel wide.

2.2.3. Statistical features (Eight feature)

In this paper, the pixel-based statistical features of the image are extracted. Statistical features are a common method of image feature extraction. Statistical features can be easily determined according to structural features. It is simple to use and apply. A total of eight features have been extracted in this feature group.

The window is used for pixel-based feature extraction. The window size used is 21x21. The reason for selecting this size is the use of 21-pixel structures on retinal blood vessel images [57]. However, this size can be changed, in other words, it is optional. The 21x21 window is move inside the ROI area. The eight features are extracted from each window. These extracted eight features are considered to be the feature of the central pixel of the respective window. Thus, pixel-based feature extraction is presented differently. In this way, the statistical feature of a window is represented by the central pixel of that window. The central pixels represent the statistical feature of the respective window. These features are as follows: arithmetic mean, minimum, maximum, skewness, kurtosis, standard deviation, mean absolute deviation.

Arithmetic Mean (μ): In the arithmetic mean, the values of all data ($p_1, p_2, \dots, p_k, \dots, p_n$) are summed. The result from the sum is divided by the total number of data (n). Thus, the arithmetic mean is calculated.

It was calculated by Eq. (7).

$$\mu = \frac{1}{n} \sum_{k=1}^n p_k \quad (7)$$

Minimum and Maximum: The minimum value is the smallest pixel value in the respective window. The maximum value is the largest pixel value in the respective window.

Skewness(S) and Kurtosis(K): Skewness was used to measure the asymmetry of the data. Kurtosis is all about the tails of the distribution. It is a measure that defines how heavily the tails of distribution differ from the tails of a normal distribution. It was calculated by Eq. (8).

$$K = \frac{\mu_4}{\sigma^4}, S = \frac{\mu_3}{\sigma^3} \quad (8)$$

Standard deviation(σ): Standard deviation is a statistic that measures the distribution relative to the mean. It is known as the square root of variance. If the data are further from the mean, there is a higher deviation within the data set. It was calculated by Eq. (9).

$$\sigma = \sqrt{\frac{1}{n} \sum_{k=1}^n (p_k - \mu)^2} \quad (9)$$

Mean absolute deviation(MAD): The MAD of the data set is the average distance between each data and the mean. It gives a piece of

information about variability in the data set. It was calculated by Eq. (10).

$$MAD = \frac{\sum |p_i - \mu|}{n} \quad (10)$$

Root sum of squared level (RSS): The RSS is of dealing with a series of values where each data is squared, the sum of these squares is calculated and the square root of that sum is then taken. It was calculated by Eq. (11)

$$RSS = \sqrt{\sum_{k=1}^n p_k^2} \quad (11)$$

2.2.4. Gradient-Based features (Four Feature)

The directional derivative of a scalar field is known as the gradient. The gradient gives a vector field that points to where the increment is greatest. A lot of information can be obtained by interpreting the gradient images of a digital image.

In Eq. 12–13, gradient vectors calculated in horizontal and vertical directions belonging to a gray level image are given. Using these vectors, gradient vector magnitude M and gradient direction θ can be calculated. Calculation of M and θ parameters in Eq. 14–15 is given.

$$G_x(x, y) = I(x+1, y) - I(x-1, y) \quad (12)$$

$$G_y(x, y) = I(x, y+1) - I(x, y-1) \quad (13)$$

$$M = |G(i, j)| = \sqrt{(G_x(i, j))^2 + (G_y(i, j))^2} \quad (14)$$

$$\theta = \tan^{-1} \left\{ (G_y(i, j) / G_x(i, j)) \right\} \quad (15)$$

The gradient feature vector used in this paper includes: G_x, G_y, M and θ . The G_x parameter is the first gradient image in the x -direction. The parameter G_y is the first gradient parameter in the y -direction. The M parameter represents the gradient magnitude and the θ parameter represents the gradient direction. The gradient magnitude improves the contrast of the blood vessels well. The θ parameter is included in the feature vector with a pixel curve.

2.2.5. Hessian matrix features (Three Features)

The matrix in which the second-order derivatives of a multivariable function are entered as elements is called the Hessian Matrix. The Hessian matrix can be used to capture the structural characteristics of retinal blood vessels. The Hessian matrix (H) is given in Eq. (16).

$$H = \begin{bmatrix} G_{xx} & G_{xy} \\ G_{yx} & G_{yy} \end{bmatrix} \quad (16)$$

The parameter G_{xx} represents the second gradient image in the x -direction. G_{xy} represents the second gradient image dependent on the y parameter in the x -direction. The parameter G_{yy} represents the second gradient parameter in the y -direction. When the second-order derivatives of the background are calculated, it has been observed that the magnitude values are small. This indicates that the second-order derivatives separate the background structure from the blood vessels [58].

2.3. Summary of feature extraction

In summary, a feature vector has been created for each pixel of retinal fundus images. This feature vector has 18-D. In total, five different feature groups were used. The green channel of the colored retinal fundus images was preprocessed and then the feature vector was created from these images. A feature has been extracted using different edge features. Representation of the features obtained from different edge detection with one feature has increased the success and saved time. The pixel-based two features were extracted using mathematical morphology. Morphological processes are effective in revealing the

Table 2
Performance measures of vessel segmentation algorithms.

Measure (Symbol)	Description	Equation
Sensitivity (Sn)/TPR	Sn ability to detect the vessel pixels.	$Sn = TP / (TP + FN)$
Specificity (Sp)/TNR	Sp ability to detect non-vessel pixels	$Sp = TN / (TN + FP)$
Accuracy (Acc)	The ratio of the total number of pixels correctly classified to the total number of pixels. This measure parameter calculated inside the field of view (FOV).	$Acc = \frac{TP + TN}{(TP + TN + FP + FN)}$
Jaccard	Jaccard similarity is used to find the similarity between two binary images.	$J(A, B) = \frac{ A \cap B }{ A \cup B }$
Dice	Dice similarity is used to find the similarity between two binary images.	$D(A, B) = \frac{2 * A \cap B }{ A + B }$

Table 3
Segmentation result of proposed method (DRIVE Dataset).

Image No.	Sn.	Sp.	Acc.	Jacc.	Dice	Running Time (s)
01_test	0.8020	0.9775	0.9625	0.6470	0.7856	32.0259
02_test	0.8730	0.9740	0.9469	0.6918	0.8178	32.0587
03_test	0.8564	0.9644	0.9559	0.6028	0.7521	33.7486
04_test	0.8798	0.9716	0.9648	0.6511	0.7887	32.9376
05_test	0.8915	0.9660	0.9608	0.6132	0.7603	34.2792
06_test	0.9046	0.9601	0.9564	0.5794	0.7337	31.3810
07_test	0.8582	0.9687	0.9607	0.6132	0.7602	32.6636
08_test	0.8578	0.9646	0.9580	0.5573	0.7157	31.5808
09_test	0.8963	0.9667	0.9628	0.5714	0.7273	33.0012
10_test	0.8497	0.9723	0.9641	0.6115	0.7589	31.5112
11_test	0.8151	0.9726	0.9602	0.6173	0.7634	32.8934
12_test	0.8476	0.9707	0.9662	0.6097	0.7576	34.4857
13_test	0.8798	0.9633	0.9572	0.5982	0.7486	34.1442
14_test	0.7664	0.9793	0.9621	0.6201	0.7655	34.2562
15_test	0.7024	0.9840	0.9612	0.5944	0.7456	33.9075
16_test	0.8600	0.9716	0.9633	0.6358	0.7773	32.0855
17_test	0.8467	0.9674	0.9597	0.5721	0.7278	33.8561
18_test	0.7814	0.9756	0.9615	0.5952	0.7462	33.5583
19_test	0.8320	0.9831	0.9709	0.6983	0.8224	34.0188
20 test	0.7998	0.9786	0.9666	0.6164	0.7627	32.1597
Average	0.8400	0.9716	0.9618	0.6148	0.7609	33.0277

Table 4
Segmentation result of proposed method (STARE Dataset).

Image No.	Sn.	Sp.	Acc.	Jaccard	Dice	Running Time (s)
Im0001. ah	0.6380	0.9782	0.9462	0.5275	0.6906	40.5045
Im0002. ah	0.5611	0.9790	0.9437	0.4569	0.6272	40.4365
Im0003. ah	0.3784	0.9904	0.9070	0.3568	0.5229	41.2735
Im0004. ah	0.7936	0.9596	0.9522	0.4268	0.5983	41.2045
Im0005. ah	0.5654	0.9727	0.9250	0.4688	0.6384	40.9699
Im0044. ah	0.6163	0.9842	0.9512	0.5309	0.6935	41.0432
Im0077. ah	0.6852	0.9911	0.9589	0.6369	0.7781	40.9554
Im0081. ah	0.6948	0.9922	0.9633	0.6478	0.7863	41.2177
Im0082. ah	0.8189	0.9892	0.9749	0.7327	0.8457	41.0351
Im0139. ah	0.5567	0.9872	0.9337	0.5107	0.6761	40.4080
Average	0.6308	0.9824	0.9456	0.5296	0.6860	40.9048

discrimination between the foreground and background of the image. Then statistical features were used and eight features were extracted. The statistical features are simple to use. It is an essential feature obtained from the image. The statistical values of the blood vessel images in the fundus images are quite different from the background. Due to this sharp difference, these features are extracted for each pixel. There are intense variations between the retinal blood vessels and the background. Therefore, a gradient between the vessel and non-vessel pixels is suspected. The magnitude of the gradient feature vector is maximum in the direction orthogonal to vessel direction. For this reason, the gradient vector has been included in the feature vector and four features have been extracted. The Hessian matrix contains the second derivative information of the image. The second derivatives emphasize zero transitions. The values of the Hessian matrix were used to access zero-crossing information of retinal blood vessels. The information of the Hessian matrix draws attention to the local curvature of the neighborhood data of each pixel of the retinal blood vessel. Hessian matrix has been included in the feature vector and three features have been extracted.

2.4. Artificial neural network

Artificial neural networks were created by inspiring from the neuron communication of the human brain. That is, it learns by using experience and data, as in the human brain. The most basic feature of ANN is its learning feature. The features extracted from each pixel of retinal fundus images are given as input to ANN. ANN starts the training process by using this information. ANN makes a generalization of the system with these examples. After the ANN training process is completed, features are extracted from each pixel of the test images of retinal fundus images. The important point here is that ANN generates the expected response to test images that it has not encountered before by using the generalization results. In this way, the segmentation stage is realized. It should be noted that too many parameters are not given during the training phase. In this case, it learns too much, that is, it becomes overfitting. If insufficient parameters are given during the training phase, it cannot learn, so it becomes under-fitting. In the proposed method, 20 training 20 test images were used for the DRIVE data set. For the STARE data set, 10 training and 10 test images were used.

The artificial neural network structure used in the proposed method is as follows: It consists of an input layer, an output layer and two hidden layers. An 18-D feature vector extracted for each pixel from retinal blood vessel images was given to the input layer. In the first and second hidden layers, the hyperbolic tangent sigmoid is used as a transfer function. Feed-forward neural network is used as the network structure.

3. Experimental results and discussion

An 18-D feature vector is extracted from each pixel for retinal blood vessel segmentation. The feature vector is extracted from 5 different feature groups. Each group has effective knowledge of the characteristic feature of the retinal blood vessel pixel. The edge detection methods positively affected the success of the experimental results. These edge features were preferred because they produced successful results in other studies. [36,58]. Statistical features were the feature group with the longest run time. Training of statistical features was completed in an average of 2195 s on the DRIVE dataset. An important point here is that feature extraction takes place during the training process. Morphological processes have a training time of 540 s, gradient-based 550 and hessian-based 1567 s, respectively. Each of these features is the classic feature used in retinal blood vessel segmentation. The segmentation success of the classical features used in the experimental results has been demonstrated. Each feature set used produced better results than complex methods. The best results for each pixel in the retinal blood vessel segmentation process were obtained when the proposed 18-D feature vector was generated. Therefore, these five feature groups (edge, morphological, statistical, gradient-based and hessian-based) were used

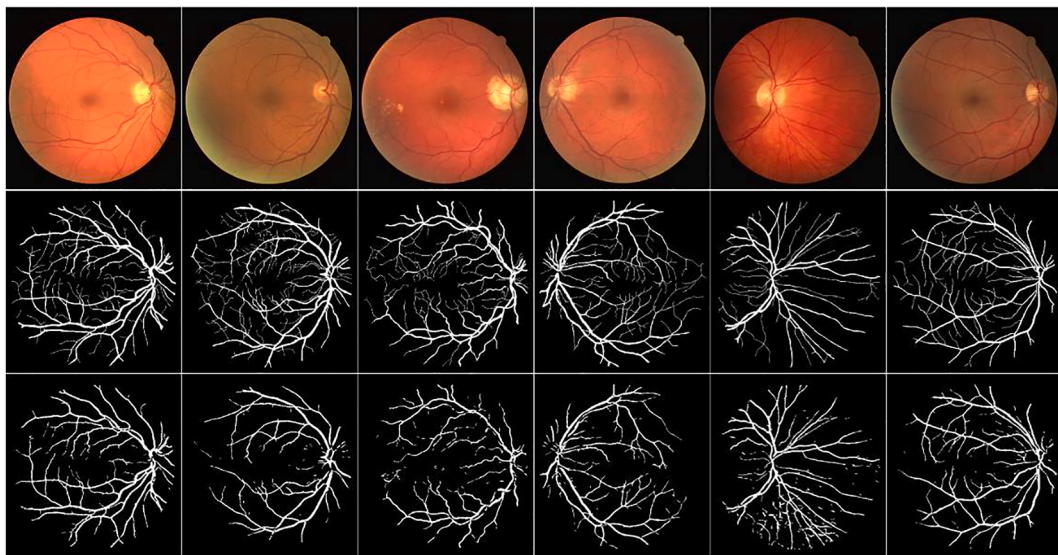


Fig. 5. Blood vessel segmentation result on DRIVE dataset. The first row is the original test images. The second row is the ground truth images. The third row is the segmentation images. The columns are '02_test', '06_test', '08_test', '12_test', '15_test' and '19_test'

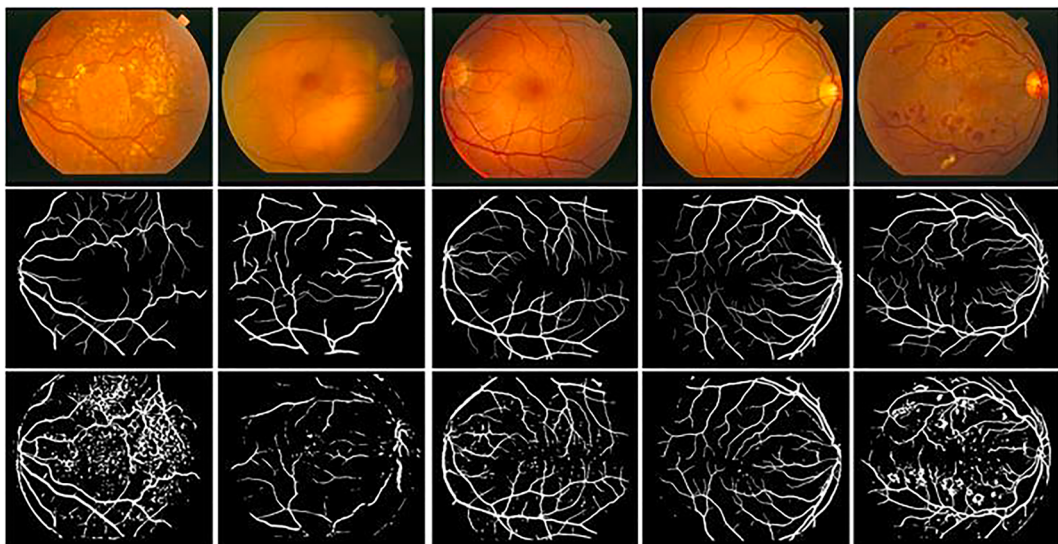


Fig. 6. Blood vessel segmentation result on STARE dataset. The first row is the original test images. The second row is the ground truth images. The third row is the segmentation images. The columns are 'Im0003', 'Im0004', 'Im0081', 'Im0082' and 'Im0139'

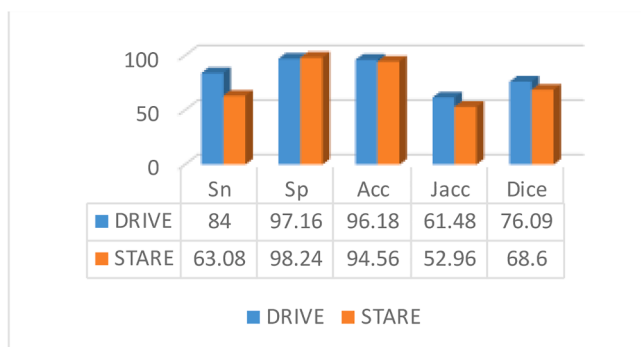


Fig. 7. Summary of performance measures



Fig. 8. Cross-training/testing segmentation average performance

Table 5

Comparison of the proposed method for DRIVE database with the state-of-art-of methods.

Year	Method	Sn. /TPR	Sp. /TNR	Acc.
2013	Odstrcilik et al. [61]	0.7807	0.9712	0.9473
2013	Wang et al. [22],	not given	not given	0.9461
2015	Roychowdhury et al. [62]	0.739	0.978	0.949
2015	Azzopardi et al. [63]	0.7655	0.9704	0.9442
2016	Anil Maharjan [64]	0.6411	0.9625	0.9349
2017	Zhu et al. [40]	0.7140	0.9868	0.9607
2017	Dash et al. [52]	0.719	0.976	0.955
2019	Yan et al. [65]	0.7631	0.9820	0.9538
2019	Sazak et al. [66]	0.718	0.981	0.959
2019	Khan et al. [67]	0.7696	0.9651	0.9506
2019	Lin et al. [68]	0.7632	not given	0.9536
2020	Tamim et al. [58]	0.7542	0.9843	0.9607
2020	Kushol et al. [69]	0.7588	0.9748	0.9456
2020	Orujov et al. [36]	0.838	0.957	0.939
2020	Shukla et al. [70]	0.7015	0.9836	0.9476
2021	Tchinda et al. [35]	0.7352	0.9775	0.9480
2021	Dikkala et al. [71]	0.6340	0.9803	0.9476
	Proposed Method	0.8400	0.9716	0.9618

Table 6

Comparison of the proposed method for STARE database with the state-of-art-of methods.

Year	Method	Sn. /TPR	Sp. /TNR	Acc.
2000	Hoover et al. [60]	0.6747	0.9384	0.9348
2006	Soares et al. [72]	0.7207	0.9747	0.9479
2011	You et al. [73]	0.7260	0.9756	0.9479
2016	Maharjan et al. [64]	0.6162	0.9615	0.9353
2019	Yan et al. [65]	0.7735	0.9857	0.9638
2019	Sazak et al. [66]	0.730	0.979	0.962
2019	Khan et al. [67]	0.7521	0.9812	0.9513
2020	Tamim et al. [58]	0.7806	0.9825	0.9632
2020	Kushol et al. [69]	0.7798	0.9746	0.9528
2020	Orujov et al. [36]	0.8342	0.8806	0.865
2020	Shukla et al. [70]	0.7023	0.9863	0.9573
2021	Tchinda et al. [35]	0.7265	0.9759	0.9548
	Proposed Method	0.6308	0.9824	0.9456

Table 7

A comparison between the Jaccard/Dice similarity index of other state-of-art-of methods.

Method	Dataset	Jaccard	Dice
Orujov et al. [36]	DRIVE	0.550	0.380
	STARE	0.3677	0.5335
Dash et al. [53]	DRIVE	0.666	0.7240
	STARE	not given	not given
Thanh et al. [74]	DRIVE	0.57355	0.72807
	STARE	not given -	not given
Proposed Method	DRIVE	0.6148	0.7609
	STARE	0.5296	0.6860

Table 8

A comparison between the average accuracy measure of other state-of-art-of methods with cross training/testing.

Year	Method	DRIVE (Trained on STARE)	STARE (Trained on DRIVE)
2006	Soares et al. [72]	0.9397	0.9327
2012	Fraz et al. [75]	0.9456	0.9495
2016	Aslani et al. [76]	0.9496	0.9545
2020	Kushol et al. [69]	0.9450	0.9487
	Proposed Method	0.9563	0.9431

in the retinal blood vessel segmentation process.

The extracted 18-D feature vector is given as input to the ANN. Eventually, the separation of the vessel and non-vessel pixels was performed. The non-vessels pixels for the DRIVE dataset are roundly 7 times the vein pixels. For the STARE dataset, this ratio is roundly 9. An important point to attention is that there are a lot of background pixels (ie non-vein pixels). Despite this class imbalance, the experimental results of the proposed method are satisfactory.

3.1. Presentation of the dataset used

The proposed method evaluated on two publicly accessible datasets. This dataset is DRIVE and STARE. These datasets consist of two manual segmentation image sets created by different experts. In the proposed method, the segmentation image of the first expert is used as the ground truth image.

The Digital Retinal Image for Vessel Extraction (DRIVE) [59] contains 40 color images of size 564×584 . These images were created randomly from a screening of 400 diabetic retinopathy patients. The ground truth image was created for each of the 40 color images by the experts. The first half of these images were selected for testing and the other half for training. Also, there are two separate expert results for the ground truth view. This paper uses the first manual expert result.

The Structured Analysis of the Retina (STARE) [60] dataset contains 20 color images of size 700×605 . The ground truth images were created for each of the 20 color images by the different two pathological experts. But, the number of training and test sets is not explicitly specified.

FOV area is used as ROI of dataset images to facilitate classifier learning and reduce learning time. The FOV field is already provided in the DRIVE dataset, but not in the STARE dataset. The FOV field was created manually in the STARE data set. The ROI is a circular shape. Thus, the margin of error is very low when creating it manually.

3.2. Presentation of the performance measures

The proposed method was evaluated using different performance measures. Segmentation image and ground truth image were evaluated using sensitivity, specificity, accuracy, Dice, and Jaccard index performance measures. In order to use these performance measures, it is necessary to know what the four basic parameters true positive (TP), true negative (TN), false positive (FP), and false negative (FN) mean. The pixel identified as the vessel in segmented retinal blood vessel images is defined as TP if it is found as the vessel in ground truth images. But, it is defined as FP if it is found as the non-vessel in ground truth images. The pixel identified as non-vessel in segmented retinal blood vessel images is defined as TN if it is found as non-vessel in ground truth images. But, it is defined as FN if it is found as the vessel in ground truth images. The performance measures used are given in Table 2.

3.3. Presenting the experimental results of the proposed method

Test results of the proposed method on the DRIVE dataset are given in Table 3. When Table 3 is examined, the maximum Sn value is 0.9046 and belongs to the '06_test' image. The minimum Sn value is 0.7024 and belongs to the '15_test' image. It is seen that the maximum Sp value belongs to the '15_test' image with 0.9840 value, and the minimum Sp value belongs to the '06_test' image with 0.9601 value. The maximum Acc value is 0.9709 and belongs to the '19_test' image. The minimum Acc value belongs to the '02_test' image with 0.9469 value. The value belonging to the maximum Jacc similarity index is 0.6983 and belongs to the '19_test' image. The value of the minimum Jacc similarity index is 0.5573 and it belongs to the '08_test' image. Finally, the maximum Dice similarity index value belongs to the '19_test' image with a value of 0.8224. The minimum Dice similarity index value belongs to the '08_test' image with a value of 0.7157. The image with the shortest segmentation time is the '06_test' image with 31.3810 s. The image with the longest

Table 9

Environmental equipment and consumption time of our method and other state-of-the-art methods. N.A: not available by their authors.

Year	Authors	Used Method	Hardware	Software	Running Time(used Dataset)
2013	Odstrcilik et al. [61]	Improved the concept of matched filtering	Intel® Core™ i7 processor, 4 GB system memory and Windows® Professional 64-bit OS.	MATLAB (R2009b)	3.22 s An average computational time of one image (DRIVE and STARE)
2013	Wang et al. [22],	Multi-wavelet kernels and multiscale hierarchical decomposition methods are used	Intel® Core™ 2 Duo CPU (3.16 GHz), 2 GB system memory and Windows XP	MATLAB	3.5 min (to process an image with seven decompositions.)
2015	Roychowdhury et al. [62]	Iterative vessel segmentation using adaptive thresholding	Intel® Core™ i3 processor, 2.6 GHz, 2-GB RAM	MATLAB	2.45 s (DRIVE) 3.9587 s (STARE)
2015	Azzopardi et al. [63]	Trainable COSFIRE filters method was used for retinal vessel delineation	2 GHz processor.	MATLAB	10 s (a singleimage from the DRIVE and STARE)
2016	Maharjan et al. [64]	A supervised method based on a neural network and moment-invariant features. An unsupervised method based on a gray-level co-occurrence matrix with local entropy. It is a matched filtering method based on the first-order derivative of Gauss.	Intel® Core™ i5, 2.6 GHz CPU with 4 GB RAM and 1 GB of dedicated GPU.	MATLAB	Around 25 min (training) and around 5 s (testing) (DRIVE and STARE)
2017	Zhu et al. [40]	Retinal vessel segmentation with pixel-based 39-D feature vector using ELM	4.0 GHz Intel i7-4790 K CPU and 32 GB memory.	MATLAB	Average 12.1602 s (DRIVE)
2017	Dash et al. [52]	Mean-C thresholding was used to extract retinal vessels	N.A	N.A	1.66 s (DRIVE)
2019	Yan et al. [65]	A tree-stage deep learning model	N.A	N.A	Not given
2019	Sazak et al. [66]	The bowler-hat transform method	Intel® Core™ i7- 4790 CPU 3.60 GHz with 16 GB RAMWindows 8.1 Pro-64 bit	MATLAB (2016b)	3.8 s (An average computational time DRIVE) 4.9 s (An average computational time STARE)
2019	Khan et al. [67]	multi-scale line detectors	Intel® i7 processor and 16 GB RAM.	MATLAB (2018a)	18.0 s (DRIVE and STARE)
2019	Lin et al. [68]	Deeply Supervised and SmoothlyRegularized Network	Caffe frameworkand NVIDIA GTX Titan X GPU	Caffe framework	12 h (training a model on a single GPU) 0.3 s (testing)
2020	Tamim et al. [58]	A supervised learning-based method using a multi-layer perceptron neural network and a 24-D feature vector	2.4 GHz Intel7-7700QH CPU and 16 GB memory using Scikit-learn	N.A	N.A (DRIVE and STARE)
2020	Kushol et al. [69]	A 4-D feature vector is constructed with the outcome of the bendlet transform	2.20 GHz processor consist of 8.00GB RAM and without any GPU	MATLAB (2015a)	N.A (DRIVE and STARE)
2020	Orujov et al. [36]	A contour detection based method based on Mamdani (Type-2) fuzzy rules	Intel® Core™ i7 (i7-2670MQ) CPU 2.0 GHz and 8 GB DDR III RAM.	Java in the Eclipse 2018-12	~1010 ms (Average execution time for DRIVE and STARE)
2020	Shukla et al. [70]	Fractional filter and eigenvalue map of a local covariance matrix was used	Intel® Core™ i36100U CPU, 2.3 GHz, 4 GB RAM	MATLAB	1.416 s (Abnormal STARE)
2021	Tchinda et al. [35]	Classical edge detection filters andthe neural network	N.A	MATLAB	N.A (DRIVE and STARE)
2021	Dikkala et al. [71]	Adaptive contrast enhancement for noise cancellation and morphological process for the extraction of features	Intel® i7 CPU at 2.20GHZ with a RAM of size 4 GB	MATLAB	30 s (Approximately processing time per image.in DRIVE)
	Proposed Method	Pixel-based feature extraction	AMD Ryzen 3 CPU at 3.10 GHz with 32 GB RAM	MATLAB	Around 20 min (training) and around 8 s (testing) (DRIVE and STARE)

segmentation time is the '12_test' image with 34.4857 s.

Test results of the proposed method on the STARE dataset are given in Table 4. When Table 4 is examined, the maximum Sn value is 0.8189 and belongs to the 'Im0082.ah' image. The minimum Sn value is 0.3784 and belongs to the 'Im0003.ah' image. It is seen that the maximum Sp value belongs to the 'Im0081.ah' image with 0.9922 value, and the minimum Sp value belongs to the 'Im0004.ah' image with 0.9596 value. The maximum Acc value is 0.9749 and belongs to the 'Im0082.ah' image. The minimum Acc value belongs to the 'Im0003.ah' image with 0.9070 value. The value belonging to the minumum $Jacc$ similarity index is 0.3568 and belongs to the 'Im0003.ah' image. The value of the maximum $Jacc$ similarity index is 0.7327 and it belongs to the 'Im0082.ah' image. Finally, the maximum $Dice$ similarity index value belongs to the 'Im0082.ah' image with a value of 0.8457. The minimum $Dice$ similarity index value belongs to the 'Im0003.ah' image with a value of 0.5229. The image with the shortest segmentation time is the 'Im0139.ah' image with 40.4080 s. The image with the longest segmentation time is the 'Im0003.ah' image with 41.2735 s. K-fold cross-validation was used to support the success of the proposed method in experimental results. Here the value of k is 10. For the DRIVE dataset, the std value for Acc, Sn, and Sp are 0.0023, 0.0240, 0.0014, respectively. For the STARE dataset, the std value for Acc, Sn, and Sp are 0.0024, 0.0299, 0.0025, respectively.

The vessel segmentation results obtained with the proposed method are shown in Fig. 5 and Fig. 6 respectively for the DRIVE and the STARE dataset. The first rows show original dataset images. The second rows show ground truth images. The third row shows the proposed method result. The results show that not only thick vessels but also thin vessels were successfully detected. The proposed method obtained more successful results in the DRIVE data set compared to the STARE data set. Fig. 5 and Fig. 6 show the images that belong to the minimum and maximum performance values obtained when the data in Table 3 and Table 4 are interpreted.

Fig. 7 shows all performance measurement values calculated for both the DRIVE data set and the STARE data set. According to this figure, although the proposed method is built independent of the data set, it is more successful in the DRIVE data set. Fig. 8 shows the average performance measures of cross-training/test segmentation results calculated for both DRIVE and STARE data set. A high accuracy rate of 95.63% was achieved when training on STARE and testing on DRIVE.

3.4. Comparison of the proposed method with state-of-the-art methods using the same dataset

Table 5 shows the performance comparison of the proposed method with other state-of-the-art methods using the DRIVE dataset. The

comparison is made between seventeen different methods from different years. Zhu et al.[40] presented a better *Sp* value than the method suggested in this paper.

Table 6 shows the comparison of the proposed method with other state-of-the-art methods using the STARE dataset. There is a point to note here. In the proposed method, the ROI field for the STARE data set was created manually. The ROI area is actually the FOV area. This situation may cause imbalance, even if it is a small amount for comparison. But it is not largely a problem. For the STARE dataset, a comparison was made between twelve different state-of-the-art methods.

Table 7 presents the comparison of Jaccard and Dice similarity index results on the DRIVE and STARE dataset with other state-of-the-art methods. The table shows the Jaccard result is lower than the Dice result. The result of Jaccard and Dice on the DRIVE dataset of the proposed method is satisfactory. **Table 8** shows a comparison of the cross-training/test result of the proposed method with other methods using the same dataset. The results of the proposed method are quite successful when testing on the STARE dataset training DRIVE dataset.

3.5. Implementation and computation time

All codes were implemented and written in MATLAB on Windows 10 64-bit PC running an AMD Ryzen 3 CPU (3.10 GHz) with 32 GB RAM. The application environments and hardware equipment of other state-of-the-art methods are given in **Table 9**.

4. Conclusion

In this paper, a method for segmenting retinal blood vessels is proposed. The proposed method is based on pixel-based feature extraction. Five different feature groups are used for feature extraction. These feature groups are edge detection methods, morphological methods, statistical methods, gradient-based methods, and hessian-based methods. Edge detection algorithms are presented as a single feature, not separately. Windows are used while extracting pixel-based statistical features. Features obtained from each window are considered as the properties of the central pixel of the respective window. A total of 18-D feature vectors was obtained. These features are given as an introduction to the ANN classifier. It realizes the training phase by using ANN training images. After the training network is created, segmentation is made on the test images. Experimental results prove that the proposed method is more successful when compared with other state-of-the-art methods. The proposed method was built independently from the dataset. However, preprocessing has been applied to all data. With the preprocessing, the noise was reduced and the light reflex was eliminated. This situation directly affects the performance success. Experimental results show that both quantitative and visual results prove that the proposed method performs relatively well. The proposed method produced robust results in different vessel structures (such as width, length, branching). The performance of the proposed method was calculated using *Sn*, *Sp* and *Acc* criteria. In addition, *Jaccard* and *Dice* index were used to calculate the similarity ratio between the segmented image and the ground truth. The proposed method provides time efficiency compared to deep learning methods, which is a popular field. For future work, we aim to find new features that increase performance and time efficiency.

Ethical approval

This article does not contain any studies with human participants or animals performed by any of the authors.

CRediT authorship contribution statement

Buket Toptaş: Software, Methodology. **Davut Hanbay:** Software, Writing - review & editing.

Declaration of Competing Interest

The authors declare that they have no known competing financial interests or personal relationships that could have appeared to influence the work reported in this paper.

Acknowledgement

This work was supported by the Inonu university scientific research and coordination unit [FDK-2020-2109]

References

- [1] M.N. Reza, Automatic detection of optic disc in color fundus retinal images using circle operator, *Biomed. Signal Process. Control.* 45 (2018) 274–283, <https://doi.org/10.1016/j.bspc.2018.05.027>.
- [2] B. Gui, R.J. Shuai, P. Chen, Optic disc localization algorithm based on improved corner detection, *Procedia Comput. Sci.* 131 (2018) 311–319, <https://doi.org/10.1016/j.procs.2018.04.169>.
- [3] A.H. Al-Sharfaa, A.Y. Yousif, E.H. Al-Saadi, Localization of Optic Disk and Exudates Detection in Retinal Fundus Images, *J. Phys. Conf. Ser.* 1804 (2021), <https://doi.org/10.1088/1742-6596/1804/1/012128>.
- [4] S.R. Rupanagudi, V.G. Bhat, B.K. Revana, J.G. Chandramouli, S. Devegowda, G. Darshan, K. Kumaran, N. Malepati, L. Manjunath, N. Shwetha, V. Ramsali, V.C. Shekar, T. M V, Y. Narayan, S. Sanjay, Optic Disk Extraction and Hard Exudate Identification in Fundus Images using Computer Vision and Machine Learning, in: 2021 IEEE 11th Annu. Comput. Commun. Work. Conf. CCWC 2021, 2021: pp. 655–661. Doi: 10.1109/CCWC51732.2021.9376018.
- [5] S. Liu, J. Hong, X. Lu, X. Jia, Z. Lin, Y. Zhou, Y. Liu, H. Zhang, Joint optic disc and cup segmentation using semi-supervised conditional GANs, *Comput. Biol. Med.* 115 (2019), <https://doi.org/10.1016/j.combiom.2019.103485>.
- [6] N. Thakur, M. Juneja, Optic disc and optic cup segmentation from retinal images using hybrid approach, *Expert Syst. Appl.* 127 (2019) 308–322, <https://doi.org/10.1016/j.eswa.2019.03.009>.
- [7] S. Yu, D. Xiao, S. Frost, Y. Kanagasingam, Robust optic disc and cup segmentation with deep learning for glaucoma detection, *Comput. Med. Imaging Graph.* 74 (2019) 61–71, <https://doi.org/10.1016/j.compmedimag.2019.02.005>.
- [8] H.N. Veena, A. Muruganandham, T. Senthil Kumar, A novel optic disc and optic cup segmentation technique to diagnose glaucoma using deep learning convolutional neural network over retinal fundus images, *J. King Saud Univ. - Comput. Inf. Sci.* (2021), <https://doi.org/10.1016/j.jksuci.2021.02.003>.
- [9] M. Niemeijer, M.D. Abràmoff, B. van Ginneken, Fast detection of the optic disc and fovea in color fundus photographs, *Med. Image Anal.* 13 (2009) 859–870, <https://doi.org/10.1016/j.media.2009.08.003>.
- [10] E.F. Kao, P.C. Lin, M.C. Chou, T.S. Jaw, G.C. Liu, Automated detection of fovea in fundus images based on vessel-free zone and adaptive Gaussian template, *Comput. Methods Programs Biomed.* 117 (2014) 92–103, <https://doi.org/10.1016/j.cmpb.2014.08.003>.
- [11] J.P. Medhi, S. Dandapat, An effective fovea detection and automatic assessment of diabetic maculopathy in color fundus images, *Comput. Biol. Med.* 74 (2016) 30–44, <https://doi.org/10.1016/j.combiom.2016.04.007>.
- [12] J.H. Tan, U.R. Acharya, S.V. Bhandary, K.C. Chua, S. Sivaprasad, Segmentation of optic disc, fovea and retinal vasculature using a single convolutional neural network, *J. Comput. Sci.* 20 (2017) 70–79, <https://doi.org/10.1016/j.jocs.2017.02.006>.
- [13] N.M. Tan, D.W.K. Wong, J. Liu, W.J. Ng, Z. Zhang, J.H. Lim, Z. Tan, Y. Tang, H. Li, S. Lu, T.Y. Wong, Automatic detection of the macula in the retinal fundus image by detecting regions with low pixel intensity, in: 2nd Int. Conf. Biomed. Pharm. Eng. ICBPE 2009 - Conf. Proc., 2009: pp. 1–5. Doi: 10.1109/ICBPE.2009.5384075.
- [14] R.J. Qureshi, L. Kovacs, B. Harangi, B. Nagy, T. Peto, A. Hajdu, Combining algorithms for automatic detection of optic disc and macula in fundus images, *Comput. Vis. Image Underst.* 116 (2012) 138–145, <https://doi.org/10.1016/j.cviu.2011.09.001>.
- [15] C. Huang, Y. Zong, Y. Ding, X. Luo, K. Clawson, Y. Peng, A new deep learning approach for the retinal hard exudates detection based on superpixel multi-feature extraction and patch-based CNN, *Neurocomputing*. (2021), <https://doi.org/10.1016/j.neucom.2020.07.145>.
- [16] N.J. Mohan, R. Murugan, T. Goel, P. Roy, Exudate Localization in Retinal Fundus Images Using Modified Speeded Up Robust Features Algorithm, in: in: *IEEE EMBS Conference on Biomedical Engineering and Sciences (IECBES)*, 2021, pp. 367–371.
- [17] M.A. Ammal, D. Gladis, Perception of hard exudates using Fuzzy Optimization and Discrete Wavelet Transformation in Fundus Image, in: Proc. Third Int. Conf. Intell. Commun. Technol. Virtual Mob. Networks (ICICV 2021), Proceedings of the Third International Conference on Intelligent Communication Technologies and Virtual Mobile Networks (ICICV 2021), 2021: pp. 1034–1039. Doi: 10.1109/icicv50876.2021.9388528.
- [18] C.A. Lupaşcu, D. Tegolo, E. Trucco, FABC: Retinal vessel segmentation using AdaBoost, *IEEE Trans. Inf. Technol. Biomed.* 14 (2010) 1267–1274, <https://doi.org/10.1109/TITB.2010.2052282>.
- [19] M. VLachos, E. Dermatas, Multi-scale retinal vessel segmentation using line tracking, *Comput. Med. Imaging Graph.* 34 (2010) 213–227, <https://doi.org/10.1016/j.compmedimag.2009.09.006>.

- [20] H. Li, J. Zhang, Q. Nie, L. Cheng, A retinal vessel tracking method based on Bayesian theory, in: Proc. 2013 IEEE 8th Conf. Ind. Electron. Appl. ICIEA 2013, IEEE, 2013; pp. 232–235. Doi: 10.1109/ICIEA.2013.65566372.
- [21] A. Fathi, A.R. Naghsh-Nilchi, Automatic wavelet-based retinal blood vessels segmentation and vessel diameter estimation, *Biomed. Signal Process. Control.* 8 (2013) 71–80, <https://doi.org/10.1016/j.bspc.2012.05.005>.
- [22] Y. Wang, G. Ji, P. Lin, E. Trucco, Retinal vessel segmentation using multiwavelet kernels and multiscale hierarchical decomposition, *Pattern Recognit.* 46 (2013) 2117–2133, <https://doi.org/10.1016/j.patcog.2012.12.014>.
- [23] P.M. Burlina, N. Joshi, M. Pekala, K.D. Pacheco, D.E. Freund, N.M. Bressler, Automated Grading of Age-Related Macular Degeneration From Color Fundus Images Using Deep Convolutional Neural Networks, *JAMA Ophthalmol.* 135 (2017) 1170–1176.
- [24] P. Burlina, D.E. Freund, B. Dupas, N. Bressler, Automatic screening of age-related macular degeneration and retinal abnormalities, *Proc. Annu. Int. Conf. IEEE Eng. Med. Biol. Soc.* (2011) 3962–3966, <https://doi.org/10.1109/EMBS.2011.6090984>.
- [25] L.K. Singh, H. Pooja, M. Garg, R.S. Khanna, Bhaduria, An enhanced deep image model for glaucoma diagnosis using feature-based detection in retinal fundus, *Med. Biol. Eng. Comput.* 59 (2021) 333–353, <https://doi.org/10.1007/s11517-020-02307-5>.
- [26] A. Shabbir, A. Rasheed, H. Shehraz, A. Saleem, B. Zafar, M. Sajid, N. Ali, S.H. Dar, T. Shehryar, Detection of glaucoma using retinal fundus images: A comprehensive review, *Math. Biosci. Eng.* 18 (2021) 2033–2076, <https://doi.org/10.1109/iCREATE.2014.6828388>.
- [27] M.H. Ahmad Fazil, L.I. Izhar, H. Nugroho, H.A. Nugroho, Analysis of retinal fundus images for grading of diabetic retinopathy severity, *Med. Biol. Eng. Comput.* 49 (2011) 693–700, <https://doi.org/10.1007/s11517-011-0734-2>.
- [28] M. Bhaskaranand, C. Ramachandran, S. Bhat, J. Cuadros, M.G. Nittala, S. Sadda, K. Solanki, Automated Diabetic Retinopathy Screening and Monitoring Using Retinal Fundus Image Analysis, *J. Diabetes Sci. Technol.* 10 (2016) 254–261, <https://doi.org/10.1177/1932296816628546>.
- [29] M. ur Rehman, Z. Abbas, S.H. Khan, S.H. Ghani, Najam, Diabetic retinopathy fundus image classification using discrete wavelet transform, in: 2018 2nd Int. Conf. Eng. Innov., 2018 2nd International Conference on Engineering Innovation (ICEI), 2018; pp. 75–80. Doi: 10.1109/icei18.2018.8448628.
- [30] J. Sahlsten, J. Jaskari, J. Kivinen, L. Turunen, E. Jaanio, K. Hietala, K. Kaski, Deep Learning Fundus Image Analysis for Diabetic Retinopathy and Macular Edema Grading, *Sci. Rep.* 9 (2019) 1–11, <https://doi.org/10.1038/s41598-019-47181-w>.
- [31] L. Math, R. Fatima, Identification of diabetic retinopathy from fundus images using CNNs, *Int. J. Innov. Technol. Explor. Eng.* 9 (2019) 3439–3443, <https://doi.org/10.35940/ijitee.A4598.119119>.
- [32] K. Narasimhan, V.C. Neha, K. Vijayarekha, Hypertensive retinopathy diagnosis from fundus images by estimation of AVR, *Procedia Eng.* 38 (2012) 980–993, <https://doi.org/10.1016/j.proeng.2012.06.124>.
- [33] M.F. Syahputra C. Amalia R.F. Rahmat D. Abdullah D. Napitupulu M.I. Setiawan W. Albra U. Nurdin Andayani, Hypertensive retinopathy identification through retinal fundus image using backpropagation neural network, in: *J. Phys. Conf. Ser.*, nd International Conference on Computing and Applied Informatics 2017, 2018. Doi: 10.1088/1742-6596/978/1/012106.
- [34] D. Nagpal, S.N. Panda, M. Malarvel, Hypertensive Retinopathy Screening through Fundus Images-A Review, *Proc. 6th Int. Conf. Inven. Comput. Technol. ICICT* (2021). (2021) 924–929, <https://doi.org/10.1109/ICICT50816.2021.9358746>.
- [35] B. Saha Tchinda, D. Tchiotsop, M. Noubom, V. Louis-Dorr, D. Wolf, Retinal blood vessels segmentation using classical edge detection filters and the neural network, *Informatics Med. Unlocked.* 23 (2021), 100521, <https://doi.org/10.1016/j.imu.2021.100521>.
- [36] F. Orujov, R. Maskeliūnas, R. Damaševičius, W. Wei, Fuzzy based image edge detection algorithm for blood vessel detection in retinal images, *Appl. Soft Comput. J.* 94 (2020), <https://doi.org/10.1016/j.asoc.2020.106452>.
- [37] T.J. Jebaseeli, C.A.D. Durai, J.D. Peter, Segmentation of retinal blood vessels from ophthalmologic Diabetic Retinopathy images, *Comput. Electr. Eng.* 73 (2019) 245–258, <https://doi.org/10.1016/j.compeleceng.2018.11.024>.
- [38] X. Wang, X. Jiang, J. Ren, Blood vessel segmentation from fundus image by a cascade classification framework, *Pattern Recognit.* 88 (2019) 331–341, <https://doi.org/10.1016/j.patcog.2018.11.030>.
- [39] H. Aguirre-Ramos, J.G. Avina-Cervantes, I. Cruz-Aceves, J. Ruiz-Pinales, S. Ledesma, Blood vessel segmentation in retinal fundus images using Gabor filters, fractional derivatives, and Expectation Maximization, *Appl. Math. Comput.* 339 (2018) 568–587, <https://doi.org/10.1016/j.amc.2018.07.057>.
- [40] C. Zhu, B. Zou, R. Zhao, J. Cui, X. Duan, Z. Chen, Y. Liang, Retinal vessel segmentation in colour fundus images using Extreme Learning Machine, *Comput. Med. Imaging Graph.* 55 (2017) 68–77, <https://doi.org/10.1016/j.compmedimag.2016.05.004>.
- [41] K. Rezaee, J. Haddadnia, A. Tashk, Optimized clinical segmentation of retinal blood vessels by using combination of adaptive filtering, fuzzy entropy and skeletonization, *Appl. Soft Comput. J.* 52 (2017) 937–951, <https://doi.org/10.1016/j.asoc.2016.09.033>.
- [42] L.C. Rodrigues, M. Marengoni, Segmentation of optic disc and blood vessels in retinal images using wavelets, mathematical morphology and Hessian-based multi-scale filtering, *Biomed. Signal Process. Control.* 36 (2017) 39–49, <https://doi.org/10.1016/j.bspc.2017.03.014>.
- [43] E. Cuevas, A. Rodríguez, A. Alejo-Reyes, C. Del-Valle-Soto, Blood Vessel Segmentation Using Differential Evolution Algorithm, Recent Metaheuristic Comput. Schemes Eng. 948 (2021) 151–167, https://doi.org/10.1007/978-3-030-66007-9_5.
- [44] M.A.U. Khan, F. Abdullah, A. Akram, R.A. Naqvi, M. Mehmood, D. Hussain, T. A. Soomro, A Scale Normalized Generalized LoG Detector Approach for Retinal Vessel Segmentation, *IEEE Access.* 9 (2021) 44442–44452, <https://doi.org/10.1109/ACCESS.2021.3063292>.
- [45] E.M. Sigursson, S. Valero, J.A. Benediktsson, J. Chanussot, H. Talbot, E. Stefánsson, Automatic retinal vessel extraction based on directional mathematical morphology and fuzzy classification, *Pattern Recognit. Lett.* 47 (2014) 164–171, <https://doi.org/10.1016/j.patrec.2014.03.006>.
- [46] B. Nayebifar, H. Abrishami Moghaddam, A novel method for retinal vessel tracking using particle filters, *Comput. Biol. Med.* 43 (2013) 541–548, <https://doi.org/10.1016/j.combiomed.2013.01.016>.
- [47] S. Chaudhuri, S. Chatterjee, N. Katz, M. Nelson, M. Goldbaum, Detection of blood vessels in retinal images using two-dimensional matched filters, *IEEE Trans. Med. Imaging.* 8 (1989) 263–269, <https://doi.org/10.1109/42.34715>.
- [48] M. Al-Rawi, H. Karajeh, Genetic algorithm matched filter optimization for automated detection of blood vessels from digital retinal images, *Comput. Methods Programs Biomed.* 87 (2007) 248–253, <https://doi.org/10.1016/j.cmpb.2007.05.012>.
- [49] M.G. Cinsikici, D. Aydin, Detection of blood vessels in ophthalmoscope images using MF/ant (matched filter/ant colony) algorithm, *Comput. Methods Programs Biomed.* 96 (2009) 85–95, <https://doi.org/10.1016/j.cmpb.2009.04.005>.
- [50] K.S. Sreejini, V.K. Govindan, Improved multiscale matched filter for retina vessel segmentation using PSO algorithm, *Egypt. Informatics J.* 16 (2015) 253–260, <https://doi.org/10.1016/j.eij.2015.06.004>.
- [51] S. Sonali, A.K. Sahu, S.P. Singh, M. Ghagra, Elhoseny, An approach for de-noising and contrast enhancement of retinal fundus image using CLAHE, *Opt. Laser Technol.* 110 (2019) 87–98, <https://doi.org/10.1016/j.optlastec.2018.06.061>.
- [52] J. Dash, N. Bhoi, A thresholding based technique to extract retinal blood vessels from fundus images, *Futur. Comput. Informatics J.* 2 (2017) 103–109, <https://doi.org/10.1016/j.fcij.2017.10.001>.
- [53] J. Dash, N. Bhoi, An Unsupervised Approach for Extraction of Blood Vessels from Fundus Images, *J. Digit. Imaging.* 31 (2018) 857–868, <https://doi.org/10.1007/s10278-018-0059-x>.
- [54] M.J. Alwazzan, M.A. Ismael, A.N. Ahmed, A Hybrid Algorithm to Enhance Colour Retinal Fundus Images Using a Wiener Filter and CLAHE, *J. Digit. Imaging.* (2021), <https://doi.org/10.1007/s10278-021-00447-0>.
- [55] K.T. Ilayaraja, E. Logashanmugam, Retinal Blood Vessel Segmentation using Morphological and Canny Edge Detection Technique, *2020 Int. Conf. Syst. Comput. Autom. Networking, ICSCAN (2020).* (2020) 1–5, <https://doi.org/10.1109/ICSCAN4926.2020.9262446>.
- [56] L.G. Roberts, Machine perception of three-dimensional solids, 1963.
- [57] M.M. Fraz, S.A. Barman, P. Remagnino, A. Hoppe, A. Basit, B. Uyyanonvara, A. R. Rudnicka, C.G. Owen, An approach to localize the retinal blood vessels using bit planes and centerline detection, *Comput. Methods Programs Biomed.* 108 (2012) 600–616, <https://doi.org/10.1016/j.cmpb.2011.08.009>.
- [58] N. Tamim, M. Elsharkawy, G.A. Azim, H. Nassar, Retinal blood vessel segmentation using hybrid features and multi-layer perceptron neural networks, *Symmetry (Basel).* 12 (2020), <https://doi.org/10.3390/SYM12060894>.
- [59] J. Staal, M.D. Abramoff, M. Niemeijer, M.A. Viergever, B. Van Ginneken, Ridge-based vessel segmentation in color images of the retina, *IEEE Trans. Med. Imaging.* 23 (2004) 501–509, <https://doi.org/10.1109/TMI.2004.825627>.
- [60] A. Hoover, Locating blood vessels in retinal images by piecewise threshold probing of a matched filter response, *IEEE Trans. Med. Imaging.* 19 (2000) 203–210, <https://doi.org/10.1109/42.845178>.
- [61] J. Odstrcilik, R. Kolar, A. Budai, J. Hornegger, J. Jan, J. Gazarek, T. Kubena, P. Cernosek, O. Svoboda, E. Angelopoulou, Retinal vessel segmentation by improved matched filtering: Evaluation on a new high-resolution fundus image database, *IET Image Process.* 7 (2013) 373–383, <https://doi.org/10.1049/iet-ipr.2012.0455>.
- [62] S. Roychowdhury, D.D. Koozekanani, K.K. Parhi, Iterative Vessel Segmentation of Fundus Images, *IEEE Trans. Biomed. Eng.* 62 (2015) 1738–1749, <https://doi.org/10.1109/TBME.2015.2403295>.
- [63] G. Azzopardi, N. Strisciuglio, M. Vento, N. Petkov, Trainable COSFIRE filters for vessel delineation with application to retinal images, *Med. Image Anal.* 19 (2015) 46–57, <https://doi.org/10.1016/j.media.2014.08.002>.
- [64] A. Maherjan, Blood vessel segmentation from retinal images, University of Eastern Finland, Faculty of Science and Forestry, Joensuu School of Computing Computer (2016), <https://doi.org/10.1109/siu.2014.6830377>.
- [65] Z. Yan, X. Yang, K. Cheng, A Three-Stage Deep Learning Model for, *EEE J. Biomed. Heal. INFORMATICS.* 23 (2019) 1427–1436.
- [66] Ç. Sazak, C.J. Nelson, B. Obara, The multiscale bowler-hat transform for blood vessel enhancement in retinal images, *Pattern Recognit.* 88 (2019) 739–750, <https://doi.org/10.1016/j.patcog.2018.10.011>.
- [67] M.A.U. Khan, J.N. Carmichael, A. Sarirete, N. Mir, Thin Vessel Detection and Thick Vessel Edge Enhancement to Boost Performance of Retinal Vessel Extraction Methods, *Procedia Comput. Sci.* 163 (2019) 618–638, <https://doi.org/10.1016/j.procs.2019.12.144>.
- [68] Y. Lin, H. Zhang, G. Hu, Automatic Retinal Vessel Segmentation via Deeply Supervised and Smoothly Regularized Network, *IEEE Access.* 7 (2019) 57717–57724, <https://doi.org/10.1109/ACCESS.2018.2844861>.
- [69] R. Kushol, M. Hasanul Kabir, M. Abdullah-Al-Wadud, M.S. Islam, Retinal blood vessel segmentation from fundus image using an efficient multiscale directional representation technique Bendlets, *Math. Biosci. Eng.* 17 (2020) 7751–7771, <https://doi.org/10.3934/MBE.2020394>.

- [70] A.K. Shukla, R.K. Pandey, R.B. Pachori, A fractional filter based efficient algorithm for retinal blood vessel segmentation, *Biomed. Signal Process. Control.* 59 (2020), 101883, <https://doi.org/10.1016/j.bspc.2020.101883>.
- [71] U. Dikkala, P. Jaya, C. Engineering, P. Jaya, A comprehensive analysis of morphological process dependent retinal blood vessel segmentation, in: *Int. Conf. Comput. Commun. Intell. Syst. A*, International Conference on Computing, Communication, and Intelligent Systems (ICCCIS) A, 2021: pp. 510–516.
- [72] J.V.B. Soares, J.J.G. Leandro, R.M. Cesar, H.F. Jelinek, M.J. Cree, Retinal vessel segmentation using the 2-D Gabor wavelet and supervised classification, *IEEE Trans. Med. Imaging.* 25 (2006) 1214–1222, <https://doi.org/10.1109/TMI.2006.879967>.
- [73] X. You, Q. Peng, Y. Yuan, Y.M. Cheung, J. Lei, Segmentation of retinal blood vessels using the radial projection and semi-supervised approach, *Pattern Recognit.* 44 (2011) 2314–2324, <https://doi.org/10.1016/j.patcog.2011.01.007>.
- [74] D.N.H. Thanh, D. Sergey, V.B. Surya Prasath, N.H. Hai, Blood vessels segmentation method for retinal fundus images based on adaptive principal curvature and image derivative operators, *Int. Arch. Photogramm. Remote Sens. Spat. Inf. Sci. - ISPRS Arch.* 42 (2019) 211–218, <https://doi.org/10.5194/isprs-archives-XLII-2-W12-211-2019>.
- [75] M.M. Fraz, P. Remagnino, A. Hoppe, B. Uyyanonvara, A.R. Rudnicka, C.G. Owen, S.A. Barman, An ensemble classification-based approach applied to retinal blood vessel segmentation, *IEEE Trans. Biomed. Eng.* 59 (2012) 2538–2548, <https://doi.org/10.1109/TBME.2012.2205687>.
- [76] S. Aslani, H. Sarnel, A new supervised retinal vessel segmentation method based on robust hybrid features, *Biomed. Signal Process. Control.* 30 (2016) 1–12, <https://doi.org/10.1016/j.bspc.2016.05.006>.